Chemical Geology 640 (2023) 121752

Contents lists available at ScienceDirect

Chemical Geology

journal homepage: www.elsevier.com/locate/chemgeo

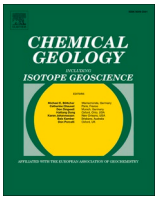

EPMA maps unveil the actual chemical variations and crystallisation sequence of pyroxene and plagioclase solidified from a basaltic liquid at variable cooling rates

Emanuela Gennaro [a,*], Francesco Radica [a,b], Gianluca Iezzi [a,b,c], Francesco Vetere [d], Manuela Nazzari [c], Georg F. Zellmer [e], Piergiorgio Scarlato [c]

[a] Dipartimento di Ingegneria e Geologia (InGeO), Università degli Studi "G. d'Annunzio", Chieti-Pescara, via dei Vestini 31, 66100 Chieti, Italy
[b] UdA-TechLab, Research Center, University "G. d'Annunzio" of Chieti-Pescara, 66100 Chieti, Italy
[c] Istituto Nazionale di Geofisica e Vulcanologia, Sezione di Roma, via di Vigna Murata 605, 00143 Roma, Italy
[d] Dipartimento di Scienze Fisiche, della Terra e dell'Ambiente, Università degli Studi di Siena, via Laterina 8, 53100 Siena, Italy
[e] Volcanic Risk Solutions, School of Agriculture and Environment, Massey University, Tennent Drive, Palmerston North 4410, New Zealand

ARTICLE INFO

Editor: Claudia Romano

Keywords:
Kinetics
Cooling rate
Basalt
Pyroxene
Plagioclase

ABSTRACT

Crystal-chemical variations of pyroxene (px) and plagioclase (plg) have been analysed by X-ray electron-microprobe (EPMA) mapping to quantify their actual chemical dispersions. These phases were experimentally crystallised from a basaltic liquid (B_{100}, MORB from Iceland) at cooling rates of 1, 7, 60 and 180 °C/h from 1300 °C down to 800 °C. Experiments were run at ambient conditions applying defined temperature paths mirroring characteristic cooling rates from innermost to outermost portions of metre- to centimetre-thick lavas, dikes and bombs emplaced under submarine to subaerial conditions. As the cooling rate increases from 1 to 180 °C/h, the run-products become progressively enriched in pyroxene and depleted in plagioclase, while spinel is invariably low (few area%) and glass is significant only at 180 °C/h. An increase of cooling rate generally leads to enrichment of Al_2O_3 and depletion of MgO in px, while the opposite behaviour is observed for plg; these trends are mirrored by calculated cations (apfu: atom per formula unit) and components. Average variations as a function of cooling rate are similar to those already observed through classical analysis performed by single point EPMA. However, the actual chemical distributions of CaO versus MgO, Al_2O_3 and FeO^{tot} oxides unveil the presence of a wider range in pyroxene chemistry. In particular, one px (px-1, CaO-rich, diopsidic type) is present at all the applied cooling rates; a very low CaO-px (px-2, pigeonite or orthopyroxene type) is detected at 1 °C/h; and, finally, once more population of px (px-3, CaO-poor diopsidic type) appears at 60 and 180 °C/h. By contrast, plg analyses yield invariably identical compositions. Textural variations as a function of cooling rate and geothermometric estimations indicate that px-1 crystallised at high-T (or low ΔT), while plg mainly grew in the residual melt produced by the saturation of px. If only textures were evaluated, this order of segregation would like remain unrecognised since px at low cooling rates is smaller than plg. The abundance of phases, their crystal-chemical features, and their order of segregation can be regarded through a theoretical framework of a time-temperature-transformation (TTT) diagram. The most significant chemical variations are displayed by MgO and Al_2O_3 for both px and plg, which faithfully capture the evolution of cooling conditions. The chemical compositions of px-1 is close to the thermodynamic *equilibrium* only at 1 °C/h. As the cooling rates increase, the px chemistry indicates *disequilibrium* conditions. Finally, this study shows that as $\Delta T/\Delta t$ increases, the most abundant px (px-1) and plg are forced towards compositions that become progressively closer to those of the parental liquid.

* Corresponding author.
E-mail address: emanuela.gennaro@unich.it (E. Gennaro).

https://doi.org/10.1016/j.chemgeo.2023.121752
Received 20 July 2023; Received in revised form 18 September 2023; Accepted 24 September 2023
Available online 29 September 2023

1. Introduction

Over the last few decades experimental studies have demonstrated that crystal-chemical and textural characteristics of minerals grown in the laboratory are able to record kinetic effects induced by variable cooling rate ($\Delta T/\Delta t$) or, in H_2O-bearing systems, degassing-induced decompression ($\Delta P/\Delta t$) rates (e.g., Hammer, 2006, 2008; Lofgren et al., 2006; Iezzi et al., 2008, 2011; Fiege et al., 2015; Mollo and Hammer, 2017; Giuliani et al., 2020a, 2020b, Giuliani et al., 2021, Giuliani et al., 2022; and references therein). The same kinetic effects are observed in volcanic rocks from outermost (rapidly chilled) to innermost (slowly cooled) portions of lavas (Hekinian et al., 2008; Lanzafame et al., 2013, 2022; McCarthy et al., 2023) or dikes (Ujike, 1982; Chistyakova and Latypov, 2009; Mollo et al., 2011; Lanzafame et al., 2017; Di Fiore et al., 2023), and during the processes of slow to rapid decompression-induced degassing experienced by hydrated magmas during their ascent in volcanic conduits (Loomis and Welber, 1982; Putirka, 2008; Cassidy et al., 2018; Kolzenburg et al., 2020; Di Fiore et al., 2022). It is thus important to thoroughly quantify these relationships in laboratory to i) obtain experimental and theoretical tools enabling the interpretation and reconstruction of solidification paths experienced by volcanic rocks and to ii) establish the degree of departure from the *equilibrium* conditions of crystallisation (Baker and Grove, 1985; Putirka, 2008; Del Gaudio et al., 2010; Mollo et al., 2010, 2011).

The kinetic effects induced by variable cooling rates are relevant for the most abundant eruptions on Earth, i.e., the effusive emplacement of tholeiitic and almost anhydrous basaltic lavas under occasionally subaerial but mainly submarine conditions (e.g., Crisp, 1984; Soule, 2015; McCarthy et al., 2023). In basaltic lavas, pyroxene (px) and plagioclase (plg) are typically the most abundant crystalline phases (Deer et al., 1992; Vetere et al., 2015) and thus prone to register variations in cooling paths followed in response to heat release from such liquids during their solidification. For an ideal basaltic liquid slice, the $\Delta T/\Delta t$ range depends on its thickness, thermal state, and type and temperature of the surrounding medium (air, seawater, country rocks); $\Delta T/\Delta t$ decreases from the outer portions of the liquid that are close to the contact with the surrounding medium, towards its inner portions (Vetere et al., 2015).

The importance of $\Delta T/\Delta t$ on crystal-chemical and textural features of crystallising plg and px in basaltic liquids prompted several studies (e.g., Baker and Grove, 1985; Del Gaudio et al., 2010; Mollo et al., 2010, 2011, 2013; Vetere et al., 2015; Giuliani et al., 2020a, 2020b, Giuliani et al., 2022). All of them highlight that progressively higher $\Delta T/\Delta t$ leads to greater degrees of *disequilibrium* crystallisation marked by a concomitant enrichment of nominal incompatible elements in the mineral phases (Lofgren et al., 2006; Hammer, 2008; Mollo and Hammer, 2017; Giuliani et al., 2022). Laboratory experiments have shown that high $\Delta T/\Delta t$ rates lead to an increase of ^{T}Al, ^{M1}Al and Na^{+} in px, while Ca^{2+} and Mg^{2+} are depleted (Mollo et al., 2010, 2011, 2013; Giuliani et al., 2022). This corresponds to a decrease of the diopsidic component (Di: $^{M2}Ca^{M1}Mg^{T}Si_2O_6$) counterbalanced by an increase of the Tschermak (CaTs: $^{M2}Ca^{M1}Al^{T}Si^{T}AlO_6$), CaFe-Tschermak (CaFeTs: $^{M2}Ca^{M1}Fe^{3+T}Si^{T}Fe^{3+}O_6$) and jadeitic (Jd: $^{M2}Na^{M1}Al^{T}Si_2O_6$) components. However, some differences in the crystal-chemistry of px are also observed as a function of the bulk alkalinity, i.e., alkaline (Mollo et al., 2010) versus sub-alkaline (Giuliani et al., 2022) basaltic systems.

With increasing cooling rates, experimental data on the alkaline basalts erupted at Mt. Etna have shown enrichments in Ti, Al, Fe^{3+}, Mg and Ca in plg corresponding to an increase of anorthite (An: $^{M}Ca^{T}Al_2^{T}Si_2O_8$) and a decrease of albite (Ab: $^{M}Na^{T}Al^{T}Si_3O_8$) and orthoclase (Or: $^{M}K^{T}Al^{T}Si_3O_8$) components (Mollo et al., 2011). On the other hand, plg crystallised from tholeiitic melts displays less pronounced or even opposite behaviours (Giuliani et al., 2022). Overall, these findings are corroborated by investigations on submarine tholeiitic basaltic flows conducted by McCarthy et al. (2023). They document that px in rapidly cooled basaltic portions are in fact characterised by enrichments of Ti, Al and Na as well as the trace elements Y, V, Ce, Zr, and Sr, and plg becomes more enriched in An content, FeO and MgO with increasing cooling rates.

Thus, px and plg are sensitive to kinetic effects such those imposed by variable $\Delta T/\Delta t$. These effects need to be better characterised in detail, because these two crystalline phases are by far the most used in petrological modelling (e.g., Putirka, 1999, 2008; Neave and Putirka, 2017). Furthermore, it should be considered that subjective punctual (or linear) selection of micro-chemical measurements through Electron Probe Microanalysis (EPMA) are able to unveil only part of the chemical variations of phases from experimental charges or natural rocks. Conversely, X-ray micro-chemical EPMA maps are able to capture the entire chemical distribution of major oxides or cations (Iezzi et al., 2014; Higgins et al., 2021; McCarthy et al., 2023; Wieser et al., 2023). Thus, the present study re-investigates through EPMA maps both px and plg grown in four experimental charges solidified from a tholeiitic mid-ocean ridge basaltic liquid. Experiments were performed by following a well-defined cooling path from 1300 °C down to 800 °C (quenching), imposing $\Delta T/\Delta t$ of 1 (3 weeks), 7 (3 days), 60 (~ 8 h) and 180 (~ 3 h) °C/h, at air P and fO_2 (Vetere et al., 2015; Giuliani et al., 2020a, 2020b; Giuliani et al., 2022). The new enlarged dataset fully unveils all the chemical features of px and plg as a function of $\Delta T/\Delta t$. The results obtained here serve as a basis for future studies using the same $\Delta T/\Delta t$ but at conditions of progressively lower fO_2 and higher P (H_2O-free and -bearing), more silicic bulk systems, as well as for px and plg grown in response to crystallisation through decompression-induced degassing ($\Delta P/\Delta t$ for H_2O-bearing systems).

2. Materials and methods

X-ray EPMA mapping was carried out on four run products solidified from dynamic experiments performed by Vetere et al. (2013, 2015), starting from the same tholeiitic liquid labelled B_{100}. The starting B_{100} glass composition was prepared using the USGS Icelandic mid-ocean ridge basalt. It was melted two times at 1600 °C for 4 h, under atmospheric P and fO_2 (Vetere et al., 2013, 2015). The bulk composition of the starting B_{100} glass is (wt%) SiO_2: 47.3(0.5), TiO_2: 1.0(0.0), Al_2O_3: 15.4(0.1), FeO^{tot}: 10.2(0.0), MnO: 0.2(0.1), MgO: 9.4(0.2), CaO: 12.8 (0.2), Na_2O: 1.9(0.1), K_2O: 0.1(0.0), while H_2O is 53 ppm and the Fe^{2+}/Fe^{3+} ratio is 0.386 (Vetere et al., 2015; Giuliani et al., 2022). Four run-products were then assembled by loading about 50 mg of B_{100} glass into Pt tubes. Subsequently, the sample charges were heated up to 1300 °C, kept at this temperature for 2 h and then cooled down to 800 °C along four $\Delta T/\Delta t$ paths of 1, 7, 60 and 180 °C/h at air P and fO_2. The quenched charges were recovered, embedded in epoxy, ground flat, polished, and carbon-coated for acquiring micro-chemical EPMA maps.

X-ray EPMA-WDS maps were acquired using the electron probe micro-analyser JEOL-JXA8200, combining EDS-WDS (equipped with five wavelength dispersive spectrometers with 12 crystals), installed at the HP-HT Laboratory of Experimental Volcanology and Geophysics of the *Instituto Nazionale di Geofisica e Vulcanologia* in Roma (Italy). The analytical strategy was set following previous studies performed on similar experimental charges with comparable textures of crystalline phases (Iezzi et al., 2014), as well as on the same run-products characterised with classical single EPMA analytical point (Giuliani et al., 2022). Each analytical point in the EPMA maps was acquired under vacuum using a focused electron beam with a diameter of <2 μm, an accelerating voltage of 15 kV, and an electric current of 10 nA. The dwell time per pixel was 120 msec, for total acquisition times between 18 h 40 min and 22 h 33 min. X-ray EPMA-WDS chemical maps were obtained by stage rastering, keeping the electron beam stationary while the stage was moved. Each collected EPMA point analysis was acquired with constant distance in each run-product at a resolution between 1 and 2 μm on run-product portions with areas between 0.25 and 1 mm^2 (Table 1).

A linear off-peak correction was used with each pixel scanned per

Table 1
Analytical conditions of chemical maps and textural attributes of px and plg.

Sample label	Cooling rate (°C/h)	Phase assemblage	Map area (mm^2)	Distance between adjacent analytical points (μm)	Number of reliable single analytical point		Area%[a]	
					px	plg	px	plg
E1	1	plg + px + sp	0.68	1.7	8850	9763	33.5 (3.9)	61.7 (5.0)
E7	7	plg + px + sp	1.00	2.0	9549	7064	34.8 (3.6)	61.6 (3.1)
E60	60	plg + px + sp	0.25	1.0	12402	3163	47.0 (3.2)	46.1 (2.4)
E180	180	px + plg + sp. + glass	0.25	1.0	33440	219	51.2 (1.4)	–

[a] The abundance of px and plg are from Giuliani et al. (2022).

element corresponding to a full quantitative analysis, attained by correcting the intensity of each analytical point for background, k factors and matrix effects. The used JEOL software permitted to export point analyses for each map on the basis of x-y coordinates. The reliability of chemical compositions obtained with EPMA maps was checked by analysing 10 single crystals for each run-product using longer counting times of 20 s on peak and 10 s on background, respectively. Differences between these two analytical methods are <1 wt% for all oxides. Thus, each point analysis or pixel of an EPMA map represents a fully quantitative determination of the major oxide components (Fig. 1S).

Multistep data screening was performed on the acquired data. First, we retained only the EPMA analyses having totals between 97.5 and 102.5 wt%. The second step of screening was based on the amounts of major elements and calculated cations (atom per formula unit, apfu) estimated for the pure phases of plg and px (Deer et al., 1992) and those estimated previously in the same run products (Giuliani et al., 2022) and from other experimental studies (Mollo et al., 2010, 2011). Cations, ferric and ferrous speciation and components (mol%) of plg and px phases were computed from measured major oxide elements (wt%) to satisfy charge balance and typical cation occupations of crystallographic sites by Si^{4+}, Ti^{4+}, Al^{3+}, Fe^{3+}, Fe^{2+}, Mg^{2+}, Ca^{2+}, K^{+} and Na^{+}. The crystal-chemical formulas of px and plg were calculated on the basis of 6 and 8 oxygens respectively (Deer et al., 1992, 2001; Morimoto, 1988). This approach corresponds to $^{M2}(Na,Ca,Fe^{2+}Mg)^{M1}(Mg,Fe^{2+},Fe^{3+},Al,Ti^{4+})^{T}(Al,Si,Ti^{4+})_2O_6$ for px (M2- and M1-sites hosting the large and lowly charged cations with a 8 and 6 coordination, respectively) and to $^{M}(K,Na,Ca,Mg)^{T}(Fe^{3+},Al,Si)_4O_8$ for plg. Only analytical points of px with both T-site and M1, 2-sites occupied by 2 ± 0.1 apfu and plg with T-site with 4 ± 0.2 apfu are considered in the following sections.

3. Results

The complete description of textural features of the four run-products is reported in previous studies (Vetere et al., 2015; Giuliani et al., 2020a, 2020b). A summary is provided through the back-scattered SEM micro-photographs displayed in Fig. 1S. In brief, run-products are characterised by the crystallisation of plg, px, sp. (spinel) and glass, plus a low amount of melilite in some run-products. According to these previous studies, px and sp. are ubiquitous in these run products, plg nucleates only at cooling rates <180 °C/h and glass is significant only at 180 °C/h (Giuliani et al., 2020a, 2022). Sp range between 3.6 and 5.4 area%, plg is the most abundant crystal in experiments performed at 1 and 7 °C/h (61.7 and 61.6 area%), then decreases at 60 °C/h (46.1 area %) and was not detected as the cooling rate approached 180 °C/h; finally, px increases from 33.5 to 51.2 area% progressively as the cooling rate increased from 1 to 180 °C/h (Table 1; Vetere et al., 2015; Giuliani et al., 2020a).

Generally, crystal size decreases and crystal number density (per area) increases from 1 to 180 °C/h, while the shape of crystals changes from faceted to dendritic between 60 and 180 °C/h (Fig. 1S; Vetere et al., 2015; Giuliani et al., 2020a). The numbers of microchemical determinations attained here using EPMA maps is on the order of a few tens of thousands for px to several thousands for plg (hundreds for run products at 180 °C/h; Table 1). Interestingly, plg was not detected in previous studies at 180 °C/h, but the EPMA maps collected here unveil its presence (see below).

3.1. Compositional variation of px

Fig. 1 plots px major oxides versus SiO_2, displaying extremely variable composition of px in all run products. As $\Delta T/\Delta t$ increases, the range of SiO_2 shrinks and decreases (42–60 vs 40–55 wt%), TiO_2 varies from 0 to 4 wt%, Al_2O_3 moves towards slightly higher amounts (0–25 vs 5–25 wt%), the FeO^{tot} range increases and shifts to higher values (0–20 vs 5–30 wt%), by contrast the MgO range shifts to lower values (5–40 vs 0–20 wt%), the CaO range narrows slightly (0–25 vs 2–25 wt%) and Na_2O varies from 0 to 6 wt% (Fig. 1). MnO and K_2O do not display significant changes, varying between 0 and 1 wt%. At low cooling rates (1 and 7 °C/h) the presence of two clusters for MgO (10–20 and 30–40 wt%) and CaO (<5 and 15–25 wt%) is observed, suggesting the coexistence of two types of px. The concurrency of MgO-rich and CaO-poor px populations suggests the presence of enstatite-type orthopyroxene or pigeonite (see below). Additionally, FeO^{tot} and Al_2O_3 at low cooling rate appear to decrease as SiO_2 increases. The average composition of analytical point clouds of SiO_2, Al_2O_3, MgO and CaO progressively converge towards the starting composition as ΔT/Δt increases (Fig. 1). These data are reported in Table 1S.

The variations of cations as a function of Si^{4+} and $\Delta T/\Delta t$ show similar features as outlined by Giuliani et al. (2022), but here, it is possible to discriminate the amount of Al in T- and M1-sites, as well as of Fe^{3+} and Fe^{2+} in M-sites (Fig. 2S). The increase of $\Delta T/\Delta t$ does not affect Ti and Na; ^{T}Al displays a perfect linear anti-correlation with Si^{4+}, suggesting that they are the unique cations in the tetrahedral site, ^{M1}Al and $^{M1}Fe^{3+}$ slightly expand their compositional ranges, $^{M}Fe^{2+}$ markedly increases its range, ^{M2}Ca slightly contracts and ^{M}Mg shrinks and also shifts to low apfu amounts (Fig. 2S). The large number of analytical points fully reveal the actual intra- (into a single crystal) and inter-crystalline (among crystals of the same phase) chemical compositions of px. The abundance of each single cation is reported in Fig. 3S. The increase of $\Delta T/\Delta t$ results in a depletion of Si^{4+} counterbalanced by an enrichment of Al in the tetrahedral site, the amounts of the Al^{tot} and ^{M1}Al also increase from 0.1 to 0.2 to 0.3–0.4 and from 0.1 to 0.2–0.3 apfu, respectively (Fig. 3S). The Fe^{3+} and Fe^{2+} cations follow complex and non-monotonic trends, Mg and Ca cations somewhat decrease, with Ca showing two peaks at 60 °C/h, and Na slightly increases (Fig. 3S). Importantly, at 1 °C/h, the Mg apfu shows an additional small peak around 1.6–1.8 apfu (Fig. 3S).

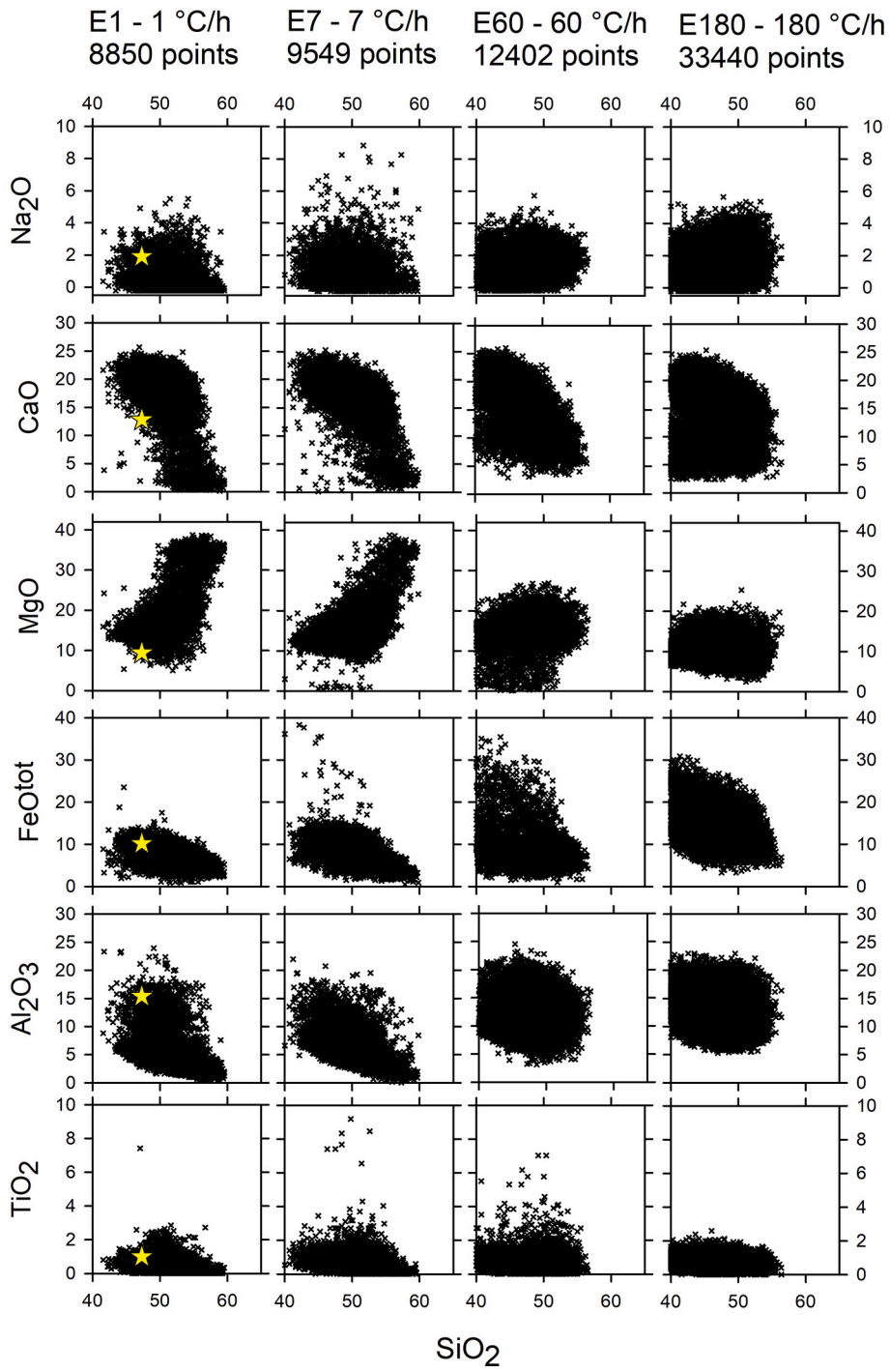

Fig. 1. Chemical variations of major oxides (wt%) in px as a function of SiO_2 content and $\Delta T/\Delta t$. Yellow star (left column) is the starting B_{100} melt composition. (For interpretation of the references to colour in this figure legend, the reader is referred to the web version of this article.)

3.2. Compositional variation of plg

Similar to px, the micro-chemical measurements of plg are also complex, with significant inter- and intra-crystalline variations of oxides (Fig. 2). The increase of $\Delta T/\Delta t$ induces a narrowing of the interval of all the major oxides and a general decrease of Al_2O_3 and CaO, counterbalanced by an increase of SiO_2 and Na_2O (Fig. 2). Plg obtained at 1 and 7 °C/h has similar CaO (0–20 wt%) and Al_2O_3 (17–35 wt%) ranges. A general increase is also shown by FeO and even more pronounced by MgO as $\Delta T/\Delta t$ increases; in detail, MgO displays a tail of compositions between 1 and 7 °C/h (Fig. 2). The amount of K_2O remains very low (< 1 wt%).

These features are mirrored by calculated cations as a function of $\Delta T/\Delta t$, with general contractions of the interval of Si, Al, Ca (except at 7 °C/h) and Na (except at 7 °C/h) ranges, whereas the ranges of Fe^{3+} and Mg remain constant between 1 and 60 °C/h and decrease between 60 and 180 °C/h (Fig. 4S). As for px, the very large amount of EPMA analytical points constrains the compositional variability of plg, but the most frequent cation abundance can be observed only through a frequency diagram with class size of 0.1 apfu (Fig. 5S). The tetrahedral site of plg is occupied mainly by Si^{4+} and Al^{3+}, and they show an opposite behaviour from 1 to 180 °C/h, with a global, but scattered, increase of

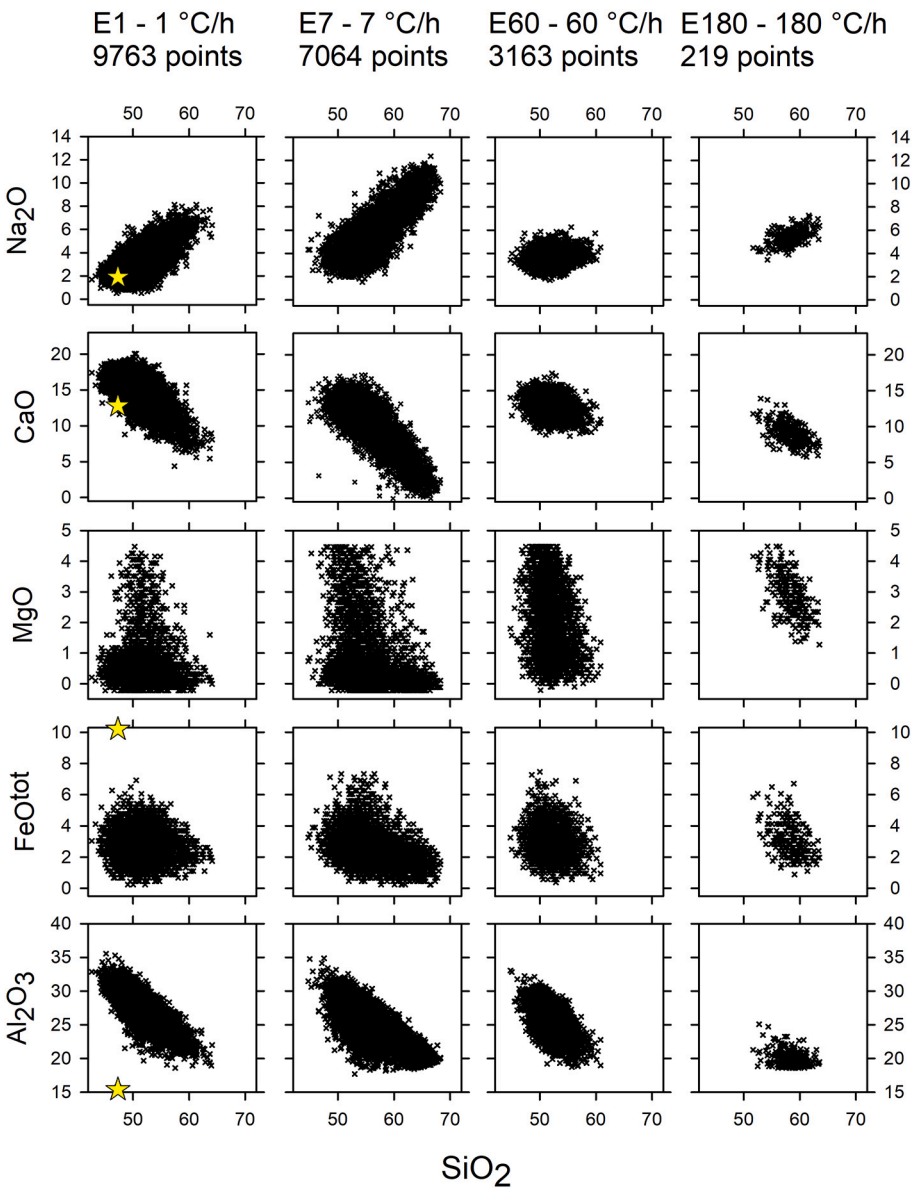

Fig. 2. Chemical variations of major oxides (wt%) in plg as function of SiO_2 content and $\Delta T/\Delta t$. Yellow star (left column) refers to the B_{100} starting melt composition. (For interpretation of the references to colour in this figure legend, the reader is referred to the web version of this article.)

Si^{4+} and decrease of Al^{3+}; Fe^{3+} contributes to achieving the ideal amount of 4 cations in the T-site (Table 2S). Similarly, Ca^{2+} and Na^{+} follow opposite trends coupled to Al^{3+} and Si^{4+}, respectively; the more abundant cation Ca^{2+} decreases from 0.8 to 0.5 apfu, while Na^{+} increases from 0.2 to 0.5 apfu as $\Delta T/\Delta t$ increases from 1 to 180 °C/h (Fig. 5S).

3.3. Px and plg components

Px compositions reveal that Di is the most abundant pole and monotonically decreases as $\Delta T/\Delta t$ increases, En slightly decreases but with a more scattered trend, whereas CaTs increases (Table 1S). Plg crystals from the four experimental charges exhibit an anorthite content of 47 to 72 mol% that decreases as the cooling rate increases, balanced by the albite content; the amount of orthoclase remains extremely low (Table 2S).

4. Discussion

4.1. EPMA single spots versus automatic maps

Comparison between single point EPMA analyses and data extracted from chemical maps is performed in terms of ^{M1}Al, ^{T}Al, Fe^{2+} and Fe^{3+} cations to evaluate crystal compositional changes. Cations from EPMA chemical maps reveal a major variability (standard deviation) in the plg and px compositions (Figs. 3 and 4) with some exceptions. For px, average abundances of Mg^{2+}, Fe^{2+} and Al^{tot} overlap between both methods, but the variability is always larger for the EPMA maps, whereas Ca^{2+}, Fe^{3+}, ^{T}Al and Si^{4+} are systematically lower and ^{M1}Al is more abundant when extracted from chemical maps (Fig. 3). For plg, the main differences between the two datasets are for Na at 1 °C/h, Ca and Si at 7 °C/h and Al at 1 and 7 °C/h (Fig. 4). Notably, the few and tiny plg crystals at 180 °C/h have been detected by chemical mapping, allowing to further expand the plg phase stability as a function of $\Delta T/\Delta t$.

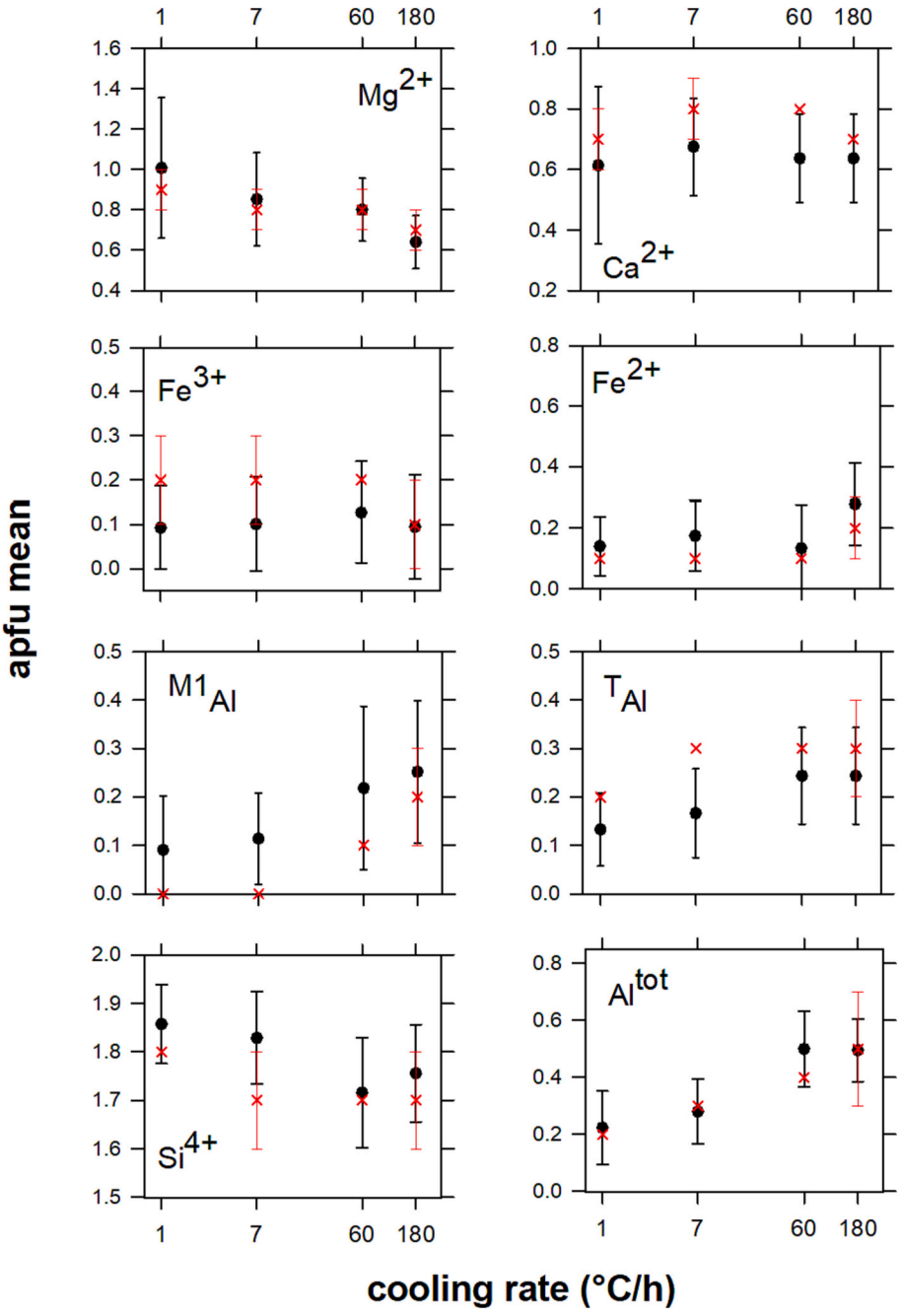

Fig. 3. Comparisons of average cations (apfu) in px from chemical mapping as a function of cooling rate obtained here by chemical maps (black circles) versus those obtained by single point analyses (red crosses, Giuliani et al., 2022). (For interpretation of the references to colour in this figure legend, the reader is referred to the web version of this article.)

4.2. Chemical variability of px and plg detected by EPMA mapping

Usually, in the absence of chemical maps, crystal compositional variations are commonly included in the associated standard deviations of average values retrieved by single analytical EPMA points or profiles (Iezzi et al., 2014; Cheng et al., 2017; Probst et al., 2018; Higgins et al., 2021).

To unveil the actual crystal-chemical dispersions displayed by px and plg, grids or heat maps of oxides (considering a step of 1 wt%) have been constructed for the chemical oxides with the largest variations, i.e. CaO vs Al_2O_3, FeO^{tot} and MgO (Fig. 5; Tables 1S and 2S). The heat maps represent the relative abundance of each px and plg oxide, also compared with the starting B_{100} liquid (Fig. 5). To have a comprehensive view, the alpaMELTS software package was used to calculate the theoretical *equilibrium* px and plg compositions at 800 °C. Briefly, the alphaMELTS (V. 1.9) software provides a simple text-based interface to subroutine versions of the MELTS algorithm (Asimow and Ghiorso, 1998, Smith and Asimow, 2005, Ghiorso et al., 2002, Ghiorso and Sack, 1991) and allows us to calculate *equilibrium* assemblages along a thermodynamic path (for details please refer to: http://melts.ofm-research.org/ and https://magmasource.caltech.edu/forum/).

One significant result displayed by heat maps is observed at 1 °C/h, where two px are present (px-1 and px-2); the first and most abundant is enriched in CaO (px-1), the less common is a CaO-, FeO- and Al_2O_3-poor and MgO-rich mineral (px-2) (Fig. 5). This confirms the frequency distribution of single Ca and Mg cations shown in Fig. 3S. The MgO-rich px

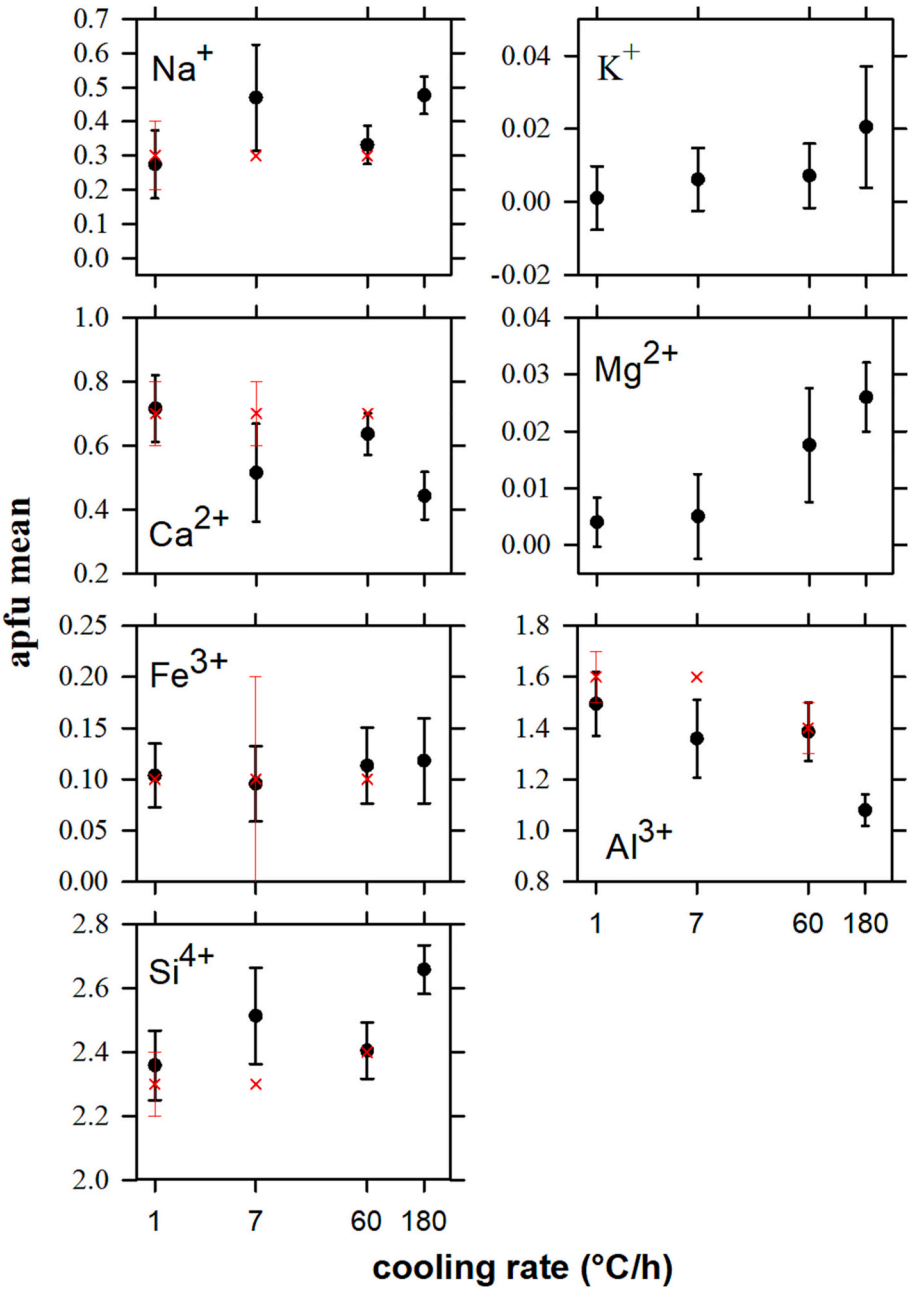

Fig. 4. Comparisons of average cations (apfu) in plg from chemical mapping as a function of cooling rate obtained here by chemical maps (black circles) versus those obtained by single point analyses (red crosses, Giuliani et al., 2022). (For interpretation of the references to colour in this figure legend, the reader is referred to the web version of this article.)

was undetected in the previous study (Giuliani et al., 2022) and explains the observed difference in the average Mg cation at 1 °C/h (Fig. 3). The MgO-rich px contains low amounts of CaO and Al_2O_3 with average values close to 3 wt% (calculated for all crystals with CaO ≤ 10 wt%), whilst MgO and FeO^{tot} averaged around 32 and 5 wt%, respectively (Table 1S). These chemical compositions may correspond to orthorhombic enstatite, monoclinic clinoenstatite or a low-CaO pigeonite (Deer et al., 1997). Since the actual distinction between orthorhombic and monoclinic chain-silicates require diffraction data (Tribaudino and Nestola, 2002), here this composition is simply referred as CaO-poor or px-2 (Fig. 5). Irrespective of its orthorhombic or monoclinic structure, MgO-rich and CaO- and FeO^{tot}-poor px typically crystallises at high-*T*, just below the liquidus temperature under *equilibrium* conditions (Grove and Juster, 1989; Deer et al., 1997). In line, the px-1 crystals (CaO > 10 wt%) are all monoclinic according to their compositions (Deer et al., 1997) (Table 1S). The plg grown at 1 °C/h is mainly clustered between 10 and 15 wt% of CaO, with a tail towards low CaO and Al_2O_3 compositions. Mirroring the shift from anorthite to albite, plg is instead richer in Al_2O_3, slightly poorer in CaO and markedly depleted in MgO- and FeO^{tot} (Fig. 5).

At 7 °C/h, there is only one population of px and one of plg. Px compositions at 7 °C/h range as follows: 15 < CaO < 22, 3 < Al_2O_3 < 10, 10 < MgO < 21 (with a notable tail towards low CaO and high MgO) and 6 < FeO^{tot} < 14 wt%. While plg shows similar features observed at 7 °C/h, although its CaO and Al_2O_3 contents are slightly lower than at 1 °C/h (Fig. 5, Tables 1S and 2S). The px-1 and plg crystallised at 7 °C/h have thus compositions similar to the px-1 and plg crystallised at 1 °C/h, but are progressively closer to the starting basaltic liquid (Fig. 5). At 60 °C/h, again two px populations are recognised; the CaO-rich population is more abundant (labelled px-1) than the CaO-poor population (labelled

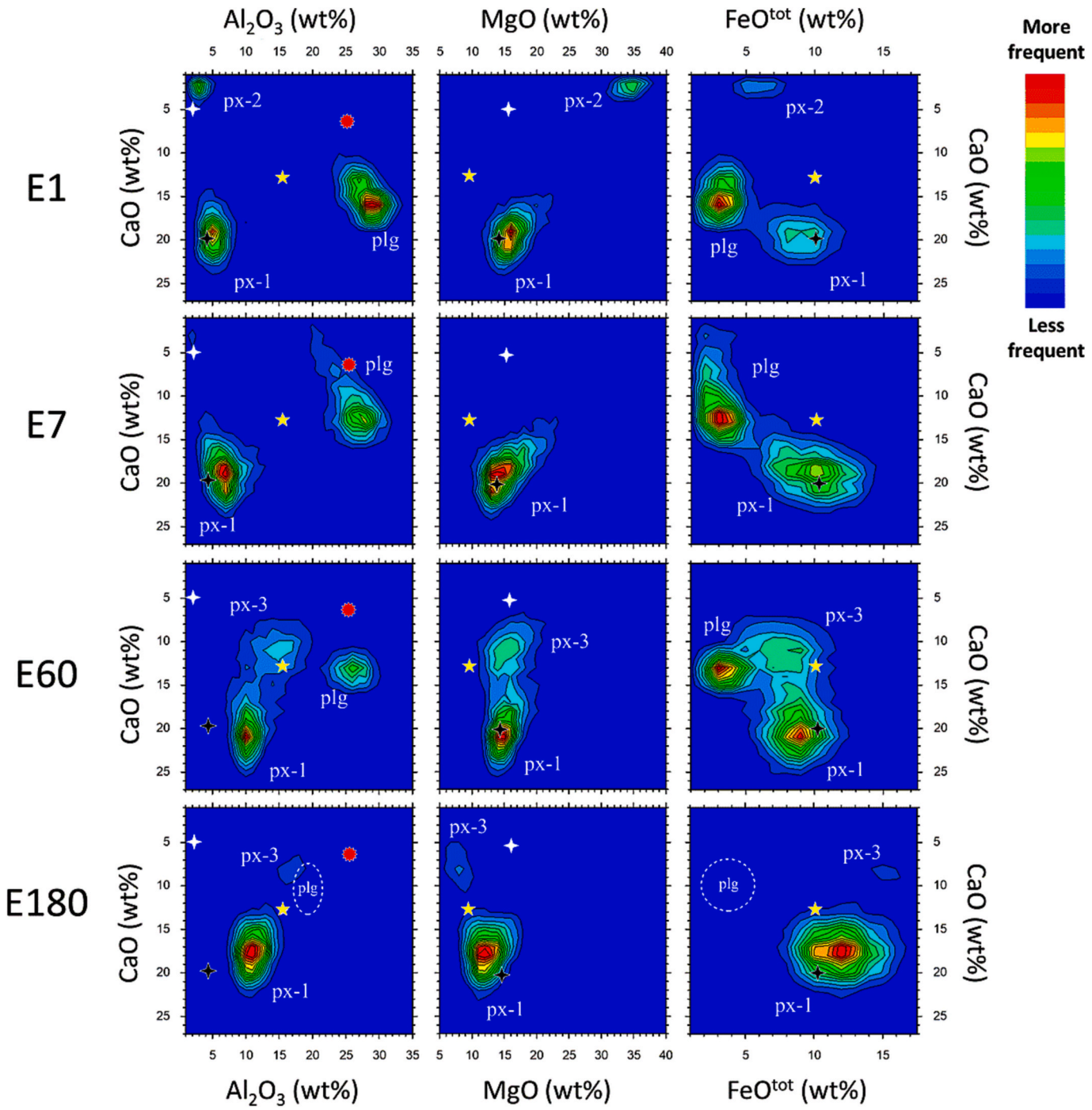

Fig. 5. Frequency of CaO versus Al_2O_3, MgO and FeO^{tot} of px and plg as a function of cooling rate. These heat maps were interpolated over a grid with bin size of 1 wt %. The px-1, px-2 and px-3 indicate the CaO-rich plus MgO-rich and CaO-poor crystals respectively (see text); the plg in E180 are marked with ellipses since their analytical points are low. The yellow star is the starting silicate melt composition (B_{100}), while black and white crosses and red sun are the two px and plg computed by alphaMELTS at *equlibrium*. (For interpretation of the references to colour in this figure legend, the reader is referred to the web version of this article.)

px-3); the former is similar to px-1 at 1 and 7 °C/h, the second is not observed in the two run-products solidified at 1 and 7 °C/h (Fig. 5, Table 1S). The plg at 60 °C/h is more clustered and less abundant than that crystallised at lower cooling rates, it is also depleted in CaO and Al_2O_3 compared to crystals formed at 7 °C/h, in agreement with its relative low area% abundance (Fig. 5, Table 2S). Finally, at the highest cooling rate of 180 °C/h, the px having CaO and Al_2O_3 compositional features similar to the other px-1 (with CaO > 12 wt%) at 1, 7 and 60 °C/h is far more abundant, whereas the CaO-poor px-3 phase (with CaO < 12 wt%) is very rare and with CaO and Al_2O_3 contents close to the very few plg (reported as ellipses in Fig. 5, Table 1S, 2S). Again, the px-1 population is more depleted in MgO and enriched in FeO^{tot} than the px-3 population (Fig. 5), while the amounts of CaO and Al_2O_3 are further reduced in plg when compared to the crystals formed at 60 °C/h.

4.3. *Textural and chemical features derived by EPMA mapping*

Identification of various px and plg populations by heat maps (Fig. 5) can be correlated with crystal textural features as displayed in Fig. 6. At 1 °C/h, the px-1 crystals are Al_2O_3-poor (blue), compositionally

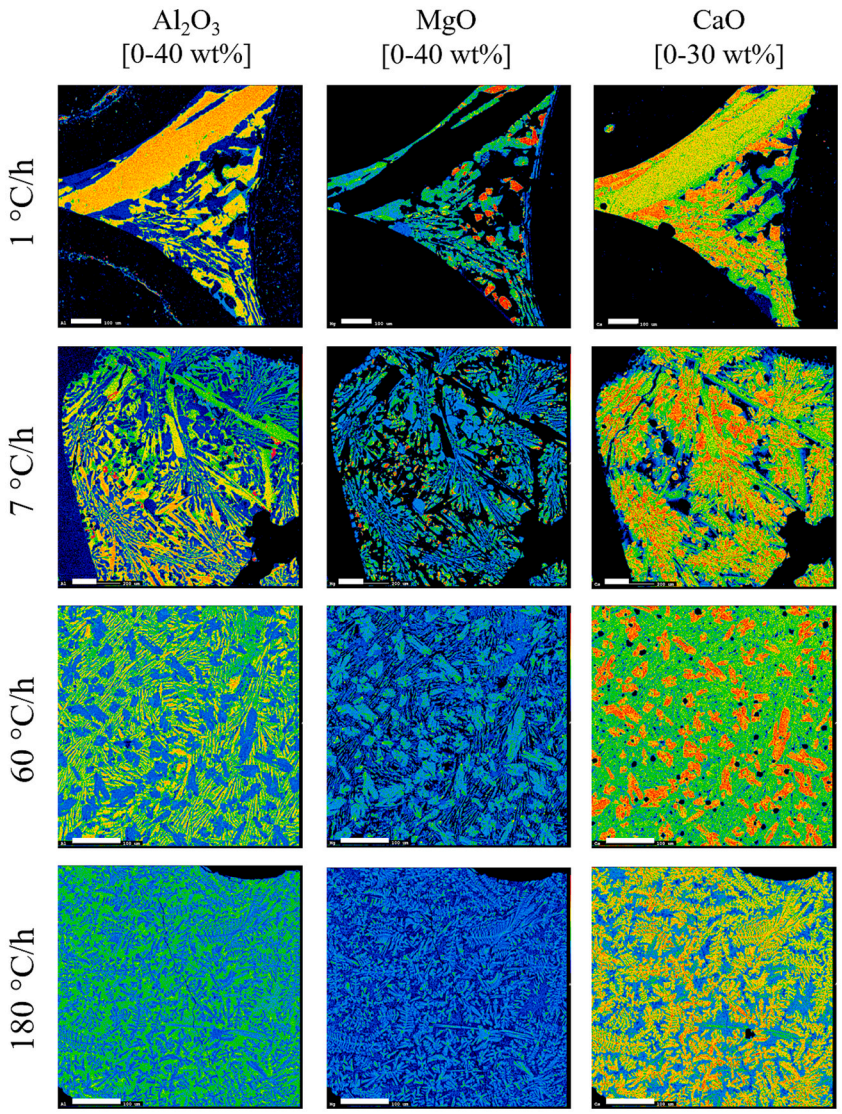

Fig. 6. EPMA maps of Al_2O_3, MgO and CaO wt% as a function of cooling rate. The horizontal white bars correspond to 100 μm. The changes from blue to red colours indicate an increase for each oxide wt% range. (For interpretation of the references to colour in this figure legend, the reader is referred to the web version of this article.)

intermediate in MgO (green) and CaO-rich (orange), the px-2 are very poor in Al_2O_3 (dark blue), MgO-rich (red) and CaO-poor (blue), and the plg are intermediate to rich in Al_2O_3 (orange to yellow), MgO-free (black) and CaO-rich (green-yellow) (Fig. 6). The most abundant px-1 crystals form an almost continuous network of relatively large and faceted crystals plus tiny and poorly faceted ones, with lengths up to 100 μm and aspect ratio (length:width) ranges from 3:1 to 5:1. The px-2 crystals are more faceted, smaller and nearly prismatic, and yield lower aspect ratios (Figs. 5 and 6). Al_2O_3-poor plg is mainly entwined with px-1 or forms very elongated large crystals (like the largest orange plg) with lengths of about 100–150 and 500 μm, respectively (Fig. 6).

At 7 °C/h, the px-1 crystals are Al_2O_3-poor (blue) and MgO-rich (green/blue) whilst plg crystals are Al_2O_3-rich (yellow/green) and MgO-free (black) (Fig. 6). In contrast to crystals formed at 1 °C/h, the shapes of px-1 and plg crystals are both strongly elongated with aspect ratios >5:1, and occasionally they develop moderate dendritic edges; px-1 and plg crystals have lengths up to 100 and 500 μm (Fig. 6), respectively. In turn, between 1 and 7 °C/h the aspect ratio increases for both px-1 and plg, while the crystal compositions become closer to the initial starting liquid (Fig. 6). At 60 °C/h, the px-1 crystals correspond to the more prismatic and large crystals with faceted to irregular edges, with the highest content of CaO (orange) (Fig. 6).

By contrast, plg and px-3 crystals are entwined and discriminable mainly in MgO and to a lesser extent in Al_2O_3 maps, whereas they are indiscriminate in CaO maps due to their very similar compositions (Fig. 5). Px-1 crystals have lengths from about 25 to 100 μm, whilst acicular px-3 and plg crystals are extremely narrow with a width of less than a few μm and lengths up to 100–150 μm (Fig. 6). Px-1 crystals at 180 °C/h have curvilinear and fern-like dendritic shapes, and are immersed in a glassy matrix; px-3 and plg crystals are scarce, extremely tiny and with overlapping CaO and Al_2O_3 compositions (Fig. 5) and thus unidentifiable at the map resolution (Fig. 6).

4.4. *Crystallisation paths of px and plg*

In line with the px and plg abundance from 1 to 9000 °C/h reported in Giuliani et al. (2020a) and Vetere et al. (2015), and with the textural relationship between spinel and px observed at high rates, the authors proposed that px nucleated after spinel, then plg crystallised after px. Additionally, px and plg estimates performed by Giuliani et al. (2022), using the thermometers proposed by Putirka (2008), unveiled that only px cores were close to *equilibrium* with the initial tholeiitic liquid,

whereas plg was always in *disequilibrium* with the starting B_{100} melt. The same test to discern between *equilibrium* and *disequilibrium* by using thermometric models by Putirka (2008) was repeated here. Results show that only a very small amount of px-1 (crystal cores) is in *equilibrium* with the initial basaltic melt, while plg is always in *disequilibrium*. Moreover, as the cooling rate increases from 1 to 60 °C/h, the fraction of px-1 with a theoretical *equilibrium* $^{cpx/melt}Kd_{Fe\text{-}Mg}$ (=0.27 ± 0.03; Putirka, 2008) is progressively less abundant, while at 180 °C/h px-1 crystals are in *disequilibrium*. The *equilibrium* px crystals return temperatures ranging from 1160 to 1220 °C (i.e., just below the estimated *liquidus* temperature of 1233 °C; Vetere et al., 2015 and Giuliani et al., 2020a).

It can thus be concluded that px-1 nucleated and typically grew earlier than plg in all run- products (Fig. 6). Hence, plg and px-3 have crystallised from the residual melt after px-1 crystallisation; in contrast, px-2 at 1 °C/h probably nucleated at very high temperatures together with px-1 (see above discussion). As a function of the amount and chemistry of px-1 and the cooling rate path, px-3 and plg were both able to crystallise almost simultaneously at 60 °C/h. Conversely, at 1 and 7 °C/h only plg solidified after the crystallisation of px-1. Since the sizes of px-1 crystals at 1 and 7 °C/h are comparable or smaller than those of plg, they could be interpreted to crystallise after plg. Indeed, in natural tholeiitic flows McCarthy et al. (2023) proposed that the larger plg invariably precipitates before the smaller px. However, here it is clearly demonstrated that smaller and/or less equant pyroxenes (px-1 and px-2) mainly grew before larger and more equant plg (Figs. 5 and 6). In addition, px-1 crystals solidified at 60 °C/h display less elongated shapes than those at 7 °C/h (Figs. 5 and 6).

These outcomes indicate that textural data unverified by chemical compositions may lead to erroneous interpretations of solidification paths. By contrast, the coupling of textural and chemical attributes (Figs. 5 and 6) allows a more robust appraisal. In parallel, sizes and shapes can be compared adequately only for the same phases, whereas comparing different crystalline structures, such as px and plg, may be inappropriate. A more confident interpretation of solidification paths is attained by the observation of natural specimens collected from the outermost (rapidly cooled) to innermost (slowly cooled) portions of lavas, pillows, dikes and bombs, or cooling rate experiments reproducing natural solidification conditions.

An additional important ramification is that px-1 and plg compositions approach to the starting liquid composition when $\Delta T/\Delta t$ increases (Figs. 1, 2 and 5). This effect reduces the atomic rearrangements required when the ions pass from the liquid to the solid state, especially for those cations having more energetic bonds with oxygen anions, such as Si (Kirkpatrick, 1981, 1983; Vetere et al., 2015). As a consequence, px-1 crystals are less reluctant to incorporate Al when the cooling rate increases, thus approaching to *equilibrium* px-1 composition computed by alphaMELTS (Fig. 5) only at 1 °C/h. More mobile cations as Ca, Mg and Fe are incorporated in the lattice site to maintain the charge-balance.

4.5. TTT diagrams

The proposed sequence of crystallisation can be interpreted in the light of time-temperature-transformation (TTT) diagrams (Johnson, 1996; Lasaga, 1998; Shelby, 2005; Wang et al., 2012; Vetere et al., 2013; Iezzi et al., 2014). This theoretical background relates the nucleation rate (I), degree of undercooling (ΔT), and nucleation induction or incubation time (τ^*), i.e., the time required to initiate nucleation of a crystalline phase (Lasaga, 1998; Fokin et al., 2003; Rusiecka et al., 2020; Di Fiore et al., 2021). Here, it is possible to quantify the phases using EPMA-maps (Figs. 5 and 6). The nucleation rate I (number of nuclei in the unit volume per second, #/(Vxt)) of silicate melts is variable, as it changes by many orders of magnitude, from the *liquidus* to the glass transition regions (T_g: here T at viscosity of 10^{12} Pa s; Lasaga, 1998; Fokin et al., 2003; Roskosz et al., 2005; Iezzi et al., 2009; Vetere et al., 2013). At the tip of a TTT curve, the nucleation rate is close to its maximum value I_{max} and to the lowest τ_{min}; consequently, as a function of the cooling rate, a silicate liquid will pierce a TTT curve at a certain temperature below its *liquidus* (i.e., ΔT corresponding also to specific values of I and τ). It is important to stress that for chemically complex magmatic silicate liquids, quantitative TTT curves are unavailable and mineral phases from magmas have stoichiometries commonly different from the parental melt (Iezzi et al., 2009; Vetere et al., 2015).

Fig. 7 shows TTT curves mirroring the cooling rates investigated here. The sluggish 1 °C/h rate intersects the TTT curve at high-T or low ΔT, at a significant τ; sp. precipitates first and induces the (perhaps heterogeneous) formation of px-1 crystals as proposed previously (Vetere et al., 2015; Giuliani et al., 2020a); again, px-2 co-precipitates together with px-1 or slightly earlier (see above). Noteworthy, the composition of px-1 (CaO-rich and Al_2O_3-poor) is close to one of the px computed by alphaMELTS (Giuliani et al., 2022), whereas that of px-2 (CaO-poor and MgO-rich) is similar to the second px computed by alphaMELTS, although it is poorer in MgO and richer in FeO (Figs. 2S, 5). With respect to the starting liquid composition and neglecting the presence of spinel, the appearance of these two pyroxenes, covering 33.5 area%, produces a significant depletion in MgO and enrichment in Al_2O_3 in the residual glass, whilst CaO and FeO^{tot} are less affected (Figs. 2 and 10). Thus, this residual melt pierces a second TTT curve where plg is able to nucleate and grow. The relatively limited chemical variability of px-1, px-2 and plg (Figs. 1 and 5) reflects crystallisation mainly due to discrete pulses, in agreement with crystallisation evolution tracked in-situ by DSC (differential scanning calorimetry) or observed in real-time by X-ray microtomography (Giuliani et al., 2020b; Polacci et al., 2018). At 7 °C/h, the scenario is similar to the 1 °C/h run-product, but the two populations of px-1 and plg are both closer to the starting composition, and px-1 chemistry is rather different from the CaO-rich pyroxene computed by alphaMELTS (Figs. 1, 5 and 6).

At 60 and 180 °C/h, the amount of px-1 increases and intersects the TTT curve at higher ΔT (low-T) and shorter τ than what observed at 1 and 7 °C/h (Table 1S, Fig. 6). Since these px-1 crystals contain less MgO and more Al_2O_3 than those found at 1 and 7 °C/h, the corresponding residual melts become respectively more enriched in MgO and depleted in Al_2O_3 than at 1 and 7 °C/h (Figs. 1, 5 and 6). At 60 °C/h, the residual melt was able to nucleate and grow some amounts of tiny and elongated px-3 and plg, whereas at 180 °C/h only a very limited amount of px-3 and plg crystallised. At 60 °C/h, the TTT curve referring to the residual melt resulting from the first pulse of nucleation of sp. and px-1 is intersected close to its nose, i.e., at I_{max} and to the lowest τ_{min}, whereas at 180 °C/h the curve is intersected far away from its nose (Fig. 7). The progressive residual melt enrichment in MgO and depletion in Al_2O_3 determines the composition of plg and px-3 crystals (Figs. 5 and 6). It is

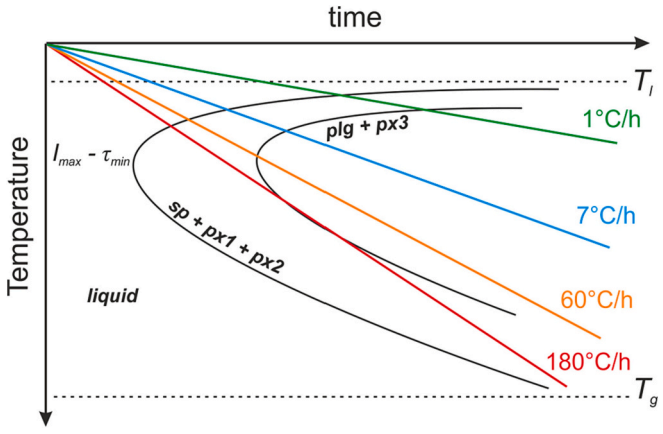

Fig. 7. Qualitative and schematic TTT diagrams referring to the crystallisation path of px and plg (see text).

important to highlight that both the 60 and 180 °C/h run-products are characterised by the presence of a glass phase, together with low amounts of melilite (Vetere et al., 2015; Giuliani et al., 2020a).

4.6. Px-1 and plg evolution as a function of cooling rate

The crystal-chemical data provided by EPMA mapping expand the range provided by the previous point analysis (Giuliani et al., 2020a) and can thus be used to gain more reliable insights into the effects of cooling kinetics. This is firstly achieved by discriminating px-1 from px-2 and px-3 populations (Figs. 5 and 6). Then, the most abundant px-1 and plg populations can be compared with the most similar experimental and natural crystals solidified at variable cooling rates in basaltic systems of similar bulk compositions. Experimental px and plg reported in Mollo et al. (2010, 2011) were solidified from an Etnean trachybasalt at 30, 126 and 180 °C/h, at ambient P and fO_2 of NNO + 1.5 and quenched at 1100 °C. The phase assemblage consists of sp., px, plg, and residual glass. A more suitable comparison to natural basaltic rocks is instead provided by the recent work of McCarthy et al. (2023). This study deals with px and plg crystallised as the groundmass of drilled submarine aphyric to highly phyric basaltic flows, containing a variable amount of plg and olivine phenocrysts, plus spinel and rare glass. The cooling rates at which px and plg grew were estimated using textural features and numerical modelling (McCarthy et al., 2023), with the

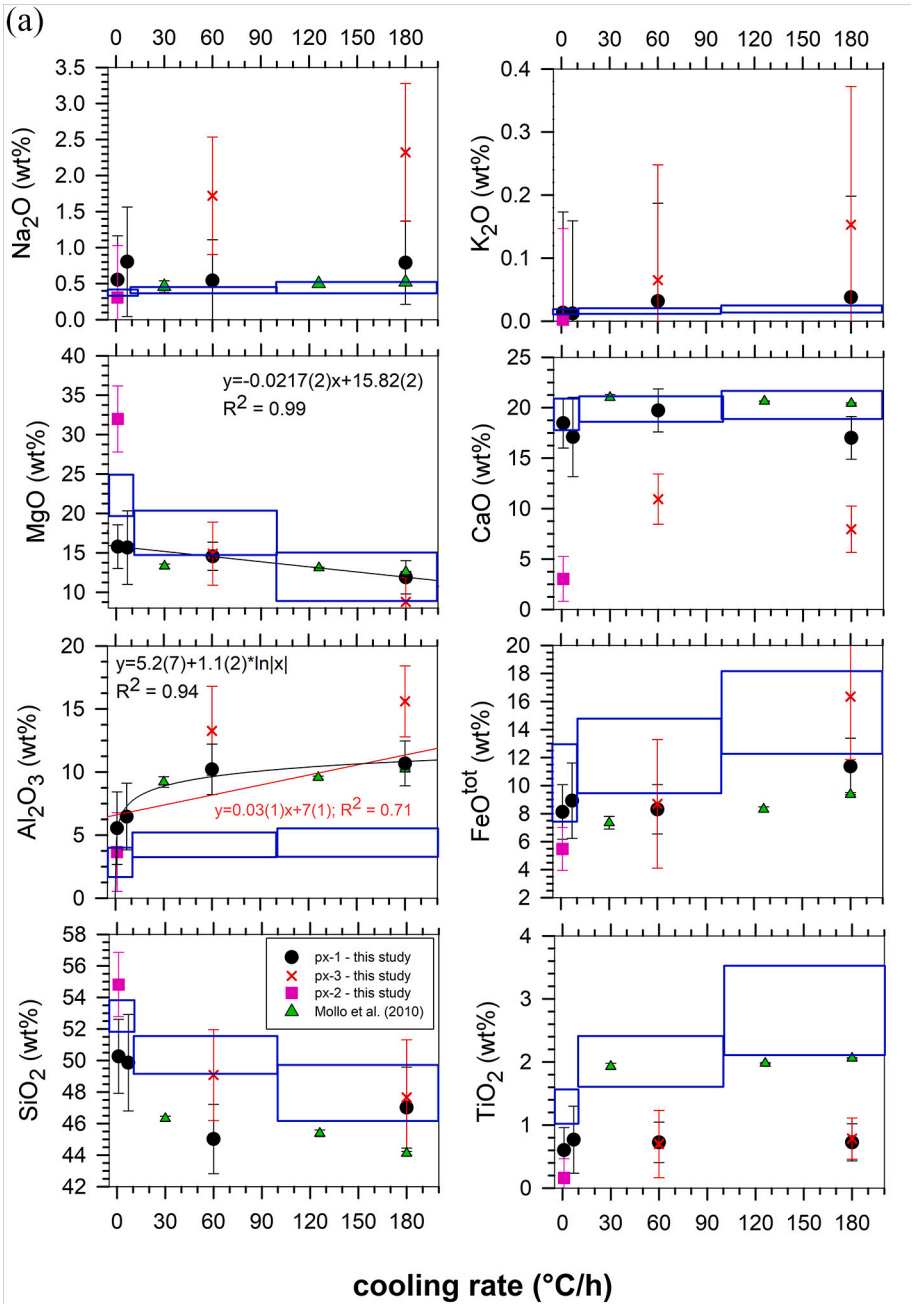

Fig. 8. a. Average oxide variations for pyroxene as function of cooling rate. Data are from this study, from previous experiments in a trachybasaltic system (green triangles, Mollo et al., 2010) and from natural basaltic flows (ranges in the blue boxes, McCarthy et al., 2023). Regressions correspond to px-1 average compositions from this study. b. Average oxide variations for plagioclase as function of cooling rate. Data are from this study, from previous experiments in a trachybasaltic system (green triangles, Mollo et al., 2011) and from natural basaltic flows (ranges in the blue boxes, McCarthy et al., 2023). Regressions correspond to plg average compositions from this study. (For interpretation of the references to colour in this figure legend, the reader is referred to the web version of this article.)

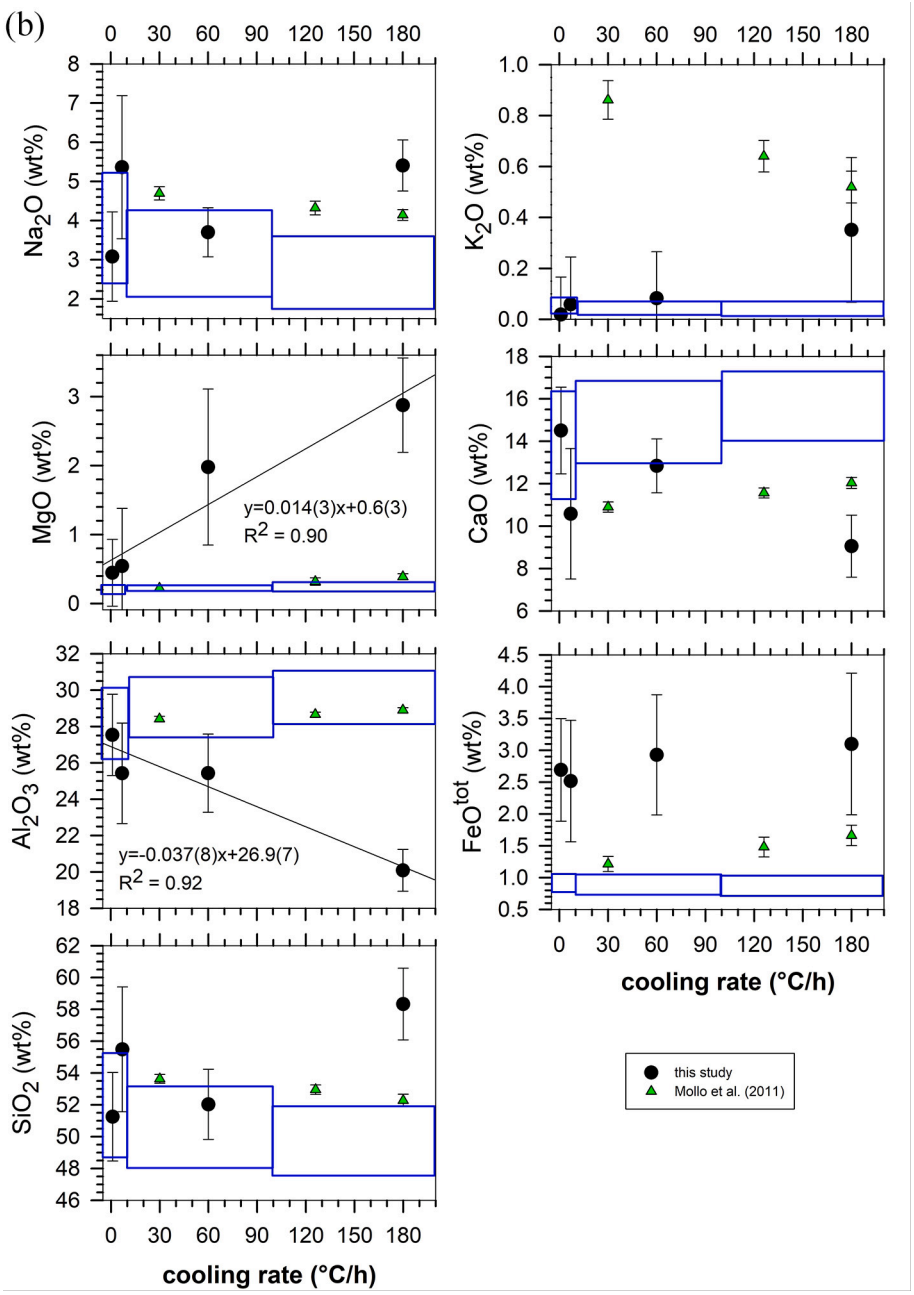

Fig. 8. (*continued*).

intention to establish three different cooling intervals of <10, between 10 and 100, and > 100 °C/h.

The major differences among the present work and those on trachybasalt (Mollo et al., 2010, 2011) and natural basaltic lavas (McCarthy et al., 2023) rely on the different compositions of silicate liquids in which px and plg grew, their low fO_2 conditions, the presence of low to moderate glass fractions and the estimation of cooling rates for natural rocks. In the limit of these differences, mineral major oxides are compared in Figs. 8, b. Note that the px (px-1) and plg reported in Mollo et al. (2010, 2011) are obtained by classical single analytical EPMA points, whereas cooling rates in McCarthy et al. (2023) are inferred to correspond to three ranges.

Px-1 crystals from this work and clinopyroxenes in synthetic trachybasalts and natural tholeiites (Mollo et al., 2010; McCarthy et al., 2023) show the same monotonically decreasing and increasing trends of MgO and Al_2O_3, respectively, whereas all other oxides present more scattered and/or limited variations (Fig. 8). For plg, MgO follows a monotonic but increasing trend, while Al_2O_3 decreases and is more scattered (crystals obtained at 7 and 60 °C/h are similar, Fig. 8b); all other oxides depict less defined trends, different from those reported by Mollo et al. (2011) and McCarthy et al. (2023). It is important to note that in our experiments, the Al_2O_3 trend in plg is opposite to that observed in both previous studies (Fig. 8b). This can be explained by the absence or very low presence of glass at 1 to 60 °C/h. Thus, plg crystals grown after the crystallisation of px-1 (and also px-2 at 1 °C/h) are able to incorporate almost all Al_2O_3 from the residual melt(s).

Hence, it is important to establish the sequence of crystallisation of px and plg in advance, before considering and quantifying kinetic effects. According to the results provided for the main population of px in all of those three basaltic melts, their cooling rate can be more robustly reconstructed using the regression analysis of MgO and Al_2O_3 (Fig. 8a). Nonetheless, the lowest amount of Al_2O_3 measured in natural samples

(McCarthy et al., 2023) will determine a lower estimate of cooling conditions. For plg, MgO is the unique oxide that shows the same increasing trend for all of the tested data sets and is thus more adequate to be used for retrieving cooling conditions according to the equation reported in Fig. 8b. Again, this equation, if applied to the plg reported in Mollo et al. (2011) and McCarthy et al. (2023), will compute cooling rates different from those experimentally used or inferred for natural conditions.

The oxide, cation and component variations in both px-1 and plg (Fig. 5, Tables 1S and 2S) as a function of cooling rate indicate a decrease of diopside and enstatite mainly counterbalanced by an increase of the Tschermak component as well as of the albite endmember. Px-1 compositional evolution again testifies a progressive departure from *equilibrium* conditions, according to the empirical tests provided in Mollo et al. (2013). If not considering the effects of cooling kinetics, geothermometer estimations on px (px-1) will provide unreliable conditions of crystallisation.

5. Concluding remarks

A detailed analytical approach based on EPMA mapping allows us to discriminate in detail the compositional evolution of silicate crystal phases during their solidification at variable cooling rates. Compared to classical single analytical EPMA spot analyses, the chemical maps provide new insights of the crystal-chemical features of crystallised phases and the relationship between textural features and crystal chemistry during the entire sequence of crystallisation.

Crystal-chemical characteristics of early nucleated phases scale with the magnitude of kinetic effects. Silicate crystals with a relatively low amount of Si (px) are more favourably crystallised and tend to occur prior to the formation of Si-rich mineral phases (plg). An increased cooling rate has the effect that nucleating phases are less able to depart from the SiO_2 content of the parental liquid and forces the concomitant incorporation of Al_2O_3, while the other oxides (FeO, MgO, CaO, Na_2O and K_2O) are used to maintain the crystal-chemical attributes of px and plg. Further, the abundance and crystal-chemistry of the first high-T (low ΔT) nucleating phase (px) determines the chemical evolution of the residual melt where further phases are forced to solidify (plg). This notion, although still not tested in depth, is probably relevant to any other natural and chemically complex silicate systems.

The experimental conditions used here (fO_2 and P of air, H_2O-free) promote a relatively high amount of Fe^{3+}. More reducing conditions (and thus lower Fe^{3+}) and higher P_{H2O} will increase chemical diffusivity and facilitate the attainment of *equilibrium* compositions of px and plg under the same experimental cooling rates imposed here. Since the px-1 compositions at 1 °C/h are similar to those calculated by theoretical *equilibrium* crystallisation (coupled to the presence of a low-CaO px), this indicates that 1 °C/h is just slightly higher than the cooling rate able to precipitate *equilibrium* px crystals. For systems richer in SiO_2 than B_{100}, the cooling rate(s) necessary to attain *equilibrium* composition(s) of the early nucleating phase(s) will be markedly lower than 1 °C/h. In turn, *disequilibrium* compositions of phases, especially at low P_{H2O} and oxidised conditions (typical of sub-marine and subaerial domains), reflect geological relevant scenarios.

The crystallisation of px affected by cooling kinetics in the basaltic melts considered in the present study was resolved by means of MgO and Al_2O_3 major component trends. For plg, MgO is the most suitable oxide to retrieve cooling conditions. Finally, TTT (time-temperature-transformation) diagrams allow us to track and interpret the solidification path of basaltic silicate liquids typical of volcanic terrestrial and extra-terrestrial rocks.

Declaration of Competing Interest

The authors declare that they have not competing financial interests or personal relationships that could have appeared to influence the work reported in this paper.

Data availability

Data are available as supplementary tables

Acknowledgments

This study was funded by the PRIN (2009PZ47NA_003) project "*Time Scales of Solidification in Magmas: Application to Volcanic Eruptions, Silicate Melts, Glasses, Glass-Ceramics*", the project "National PNRR- MUR, DM. 1062 (10/08/2021), REACT-EU - PON R&I 2014-2020 - "*Azione IV.4 Contratti di Ricerca su tematiche Green*" and the "*Fondi Ateneo of the University G. D'Annunzio*" all awarded to G. Iezzi.

Appendix A. Supplementary data

Supplementary data to this article can be found online at https://doi.org/10.1016/j.chemgeo.2023.121752.

References

Asimow, P.D., Ghiorso, M.S., 1998. Algorithmic modifications extending MELTS to calculate subsolidus phase relations. Am. Mineral. 83, 1127–1132.
Baker, M.B., Grove, T.L., 1985. Kinetic controls on pyroxene nucleation and metastable liquid lines of descendent in a basaltic andesite. Am. Mineral. 70, 279–287.
Cassidy, M., Manga, M., Cashman, K., Bachmann, O., 2018. Controls on explosive-effusive volcanic eruption styles. Nat. Commun. 9, 2839. https://doi.org/10.1038/s41467-018-05293-3.
Cheng, L., Costa, F., Carniel, R., 2017. Unraveling the presence of multiple plagioclase populations and identification of representative two-dimensional sections using a statistical and numerical approach. Am. Mineral. 102, 1894–1905.
Chistyakova, S., Latypov, R., 2009. On the development of internal chemical zonation in small mafic dikes. Geol. Mag. 147, 1–12.
Crisp, J.A., 1984. Rates of magma emplacement and volcanic output. J. Volcanol. Geotherm. Res. 20, 177–211. https://doi.org/10.1016/0377-0273(84)90039-8.
Deer, W.A., Howie, R.A., Zussmann, J., 1992. An Introduction to the Rock-forming Minerals, 2nd edition. Longman, Harlow. (696 pp).
Deer, W.A., Howie, R.A., Zussman, J., 1997. Single-chain Silcates, second edition. The Geological Society, London.
Deer, W.A., Howie, R.A., Zussman, J., 2001. Framework Silicates: Feldspars, second edition. The Geological Society, London.
Del Gaudio, P., Mollo, S., Ventura, G., Iezzi, G., Taddeucci, J., Cavallo, A., 2010. Cooling rate-induced differentiation in anhydrous and hydrous basalts at 500 MPa: implications for the storage and transport of magmas in dikes. Chem. Geol. 270, 164–178.
Di Fiore, F., Vona, A., Kolzenburg, S., Mollo, S., Romano, C., 2021. An Extended Rheological Map of Pāhoehoe—'a'ā transition. J Geophys. Res. Solid Earth 126, 1–23. https://doi.org/10.1029/2021JB022035.
Di Fiore, F., Vona, A., Costa, A., Mollo, S., Romano, C., 2022. Quantifying the influence of cooling and shear rate on the disequilibrium rheology of a trachybasaltic melt from Mt. Etna. Earth Planet. Sci. Lett. 594, 117725. https://doi.org/10.1016/j.epsl.2022.117725.
Di Fiore, F., Vona, A., Scarani, A., Giordano, G., Romano, C., Giordano, D., Caricchi, L., Martin Lorenzo, A., Rodriguez, F., Coldwell, B., Hernandez, P., Pankhurst, M., 2023. Experimental Constraints on the Rheology of Lavas from 2021 Cumbre Vieja Eruption (La Palma, Spain). Geophys. Res. Lett. 50 https://doi.org/10.1029/2022GL100970.
Fiege, A., Vetere, F., Iezzi, G., Simon, A., Holtz, F., 2015. The roles of decompression rate and volatiles (H_2O + Cl ± CO_2 ± S) on crystallization in (trachy-) basaltic magma. Chem. Geol. 411, 310–322.
Fokin, V.M., Zanotto, E.D., Schmelzer, J.W.P., 2003. Homogeneous nucleation versus glass transition temperature of silicate glasses. J. Non Cryst. Solids 321, 52–65.
Ghiorso, M.S., Sack, R.O., 1991. Fe-Ti oxide geothermometry: thermodynamic formulation and the estimation of intensive variables in silicic magmas. Contrib. Mineral. Petrol. 108, 485–510.
Ghiorso, M.S., Hirschmann, M.M., Reiners, P.W., Kress, V.C., 2002. The pMELTS: a revision of MELTS for improved calculation of phase relations and major element partitioning related to partial melting of the mantle to 3 GPa. Geochem. Geophys. Geosyst. 3, 1030.
Giuliani, L., Iezzi, G., Vetere, F., Behrens, H., Mollo, S., Cauti, F., Ventura, G., Scarlato, P., 2020a. Evolution of textures, crystal size distributions and growth rates of plagioclase, clinopyroxene and spinel solidified at variable cooling rates from a mid-ocean ridge basaltic liquid. Earth Sci. Rev. 204, 103165.
Giuliani, L., Iezzi, G., Hippeli, T., Davis, M., Elbrecht, A., Vetere, F., Nazzari, M., Mollo, S., 2020b. The onset and solidification path of a basaltic melt by in situ differential scanning calorimetry (DSC) and ex situ investigations. Front. Earth Sci. 8, 337. https://doi.org/10.3389/feart.2020.00337.

Giuliani, L., Iezzi, G., Mollo, S., 2021. Dynamics of volcanic systems: physical and chemical models applied to equilibrium versus disequilibrium solidification of magmas. In: Vetere, F. (Ed.), AGU Geophysical Monograph Series: Dynamic Magma Evolution. American Geophysical Union, pp. 99–132. https://doi.org/10.1002/9781119521143.ch5.

Giuliani, L., Vetere, F., Iezzi, G., Nazzari, M., Mollo, S., Behrens, H., Scarlato, P., Ventura, G., 2022. Crystal-chemical variations of spinel, clinopyroxene, and plagioclase in MORB basaltic melt induced by continuous cooling. Chem. Geol. 594, 120765.

Grove, T.L., Juster, T.C., 1989. Experimental investigations of low-Ca pyroxene stability and olivine- pyroxene- liquid equilibria at 1-atm in natural basaltic and andesitic liquids. Contrib. Mineral. Petrol. 103, 287–305.

Hammer, J.E., 2006. Influence of fO_2 and cooling rate on the kinetics and energetics of Fe-rich basalt crystallization. Earth Planet. Sci. Lett. 248, 618–637.

Hammer, J.E., 2008. Experimental studies of the kinetics and energetics of magma crystallization. In: Putirka, K.D., Tepley, F.J. (Eds.), Minerals, Inclusions and Volcanic Processes, Reviews in Mineralogy and Geochemistry, vol. 69. Chantilly, VA, Mineralogical Society of America, pp. 9–59.

Hekinian, R., Mühe, R., Worthington, T.J., Stoffers, P., 2008. Geology of a submarine volcanic caldera in the Tonga Arc: dive results. J. Volcanol. Geotherm. Res. 176, 571–582.

Higgins, O., Sheldrake, T., Caricchi, L., 2021. Quantitative chemical mapping of plagioclase as a tool for the interpretation of volcanic stratigraphy: an example from Saint Kitts, Lesser Antilles. Bull. Volcanol. 83, 51. https://doi.org/10.1007/s00445-021-01476-x.

Iezzi, G., Mollo, S., Ventura, G., Cavallo, A., Romano, C., 2008. Experimental solidification of anhydrous latitic and trachytic melts at different cooling rates: the role of nucleation kinetics. Chem. Geol. 253, 91–101.

Iezzi, G., Mollo, S., Ventura, G., 2009. Solidification behaviour of natural silicate melts and volcanological implications. In: Lewis, N., Moretti, A. (Eds.), Volcanoes: Formation, Eruptions and Modelling. Nova Publishers, New York, NY, pp. 127–151.

Iezzi, G., Mollo, S., Torresi, G., Ventura, G., Cavallo, A., Scarlato, P., 2011. Experimental solidification of an andesitic melt by cooling. Chem. Geol. 283, 261–273.

Iezzi, G., Mollo, S., Shahini, E., Cavallo, A., Scarlato, P., 2014. Investigating Petrologic indicators of Magmatic Processes in Volcanic Rocks, the cooling kinetics of plagioclase feldspar as revealed by electron-microprobe mapping. American Mineralogist 99, 898–907.

Johnson, W.L., 1996. Fundamental aspects of bulk metallic glass formation in multicomponent alloys. Mater. Sci. Forum 225–227, 35–50.

Kirkpatrick, R.J., 1981. Kinetics of crystallization of igneous rocks. In: Lasaga, A.C., Kirckpatrick, R.J. (Eds.), Rev. Mineral. Geochem, 8, pp. 321–397.

Kirkpatrick, R.J., 1983. Theory of nucleation in silicate melts. Am. Mineral. 68, 66–77.

Kolzenburg, S., Hess, K.U., Berlo, K., Dingwell, D.B., 2020. Disequilibrium rheology and crystallization kinetics of basalts and implications for the Phlegrean Volcanic District. Front. Earth Sci. 8, 187. https://doi.org/10.3389/feart.2020.00187.

Lanzafame, G., Mollo, S., Iezzi, G., Ferlito, C., Ventura, G., 2013. Unravelling the solidification path of a pahoehoe "cicirara" lava from Mount Etna volcano. Bull. Volcanol. 75-4, 1–16.

Lanzafame, G., Iezzi, G., Mancini, L., Lezzi, F., Mollo, S., Ferlito, C., 2017. Solidification and turbulence (non-laminar) during magma ascent: insights from 2D and 3D analyses of bubbles and minerals in an Etnean dyke. J. Petrol. 58 (8), 1511–1533.

Lanzafame, G., Giacomoni, P.P., Casetta, G., Mancini, L., Iezzi, G., Coltorti, M., Ferlito, C., 2022. Degassing, crystallization and rheology of hawaiitic lava flows: the case of the 1669 A.D. eruption of Mount Etna (Italy). Journal of Petrology 63, 115. https://doi.org/10.1093/petrology/egac115.

Lasaga, A.C., 1998. Kinetic Theory in the Earth Sciences. Princeton University Press, Princenton, New York.

Lofgren, G.E., Huss, G.R., Wasserburg, G.J., 2006. An experimental study of trace-element partitioning between Ti-Al-clinopyroxene and melt: equilibrium and kinetic effects including sector zoning. Am. Mineral. 91, 1596–1606.

Loomis, T.P., Welber, P.W., 1982. Crystallization processes in the rocky hill granodiorite pluton, California: an interpretation based on compositional zoning of plagioclase. Contrib. Min. Petrol. 81, 230–239.

McCarthy, A., Chelle-Michou, C., Blundy, J.D., Dorais, M.J., van der Zwan, F.M., Peate, D.W., 2023. The effect of variations in cooling rates on mineral compositions in mid-ocean ridge basalts. Chem. Geol. 625, 121415. https://doi.org/10.1016/j.chemgeo.2023.121415.

Mollo, S., Hammer, J.E., 2017. Dynamic crystallization in magmas. EMU Notes in Mineralogy 16, 373–418. https://doi.org/10.1180/EMU-notes.16.12.

Mollo, S., Del Gaudio, P., Ventura, G., Iezzi, G., Scarlato, P., 2010. Dependence of clinopyroxene composition on cooling rate in basaltic magmas: implications for thermobarometry. Lithos 118, 302–312.

Mollo, S., Lanzafame, G., Masotta, M., Iezzi, G., Ferlito, C., Scarlato, P., 2011. Cooling history of a dike as revealed by mineral chemistry: a case study from Mt. Etna volcano. Chemical Geology 2011 (288), 39–52.

Mollo, S., Putirka, K., Iezzi, G., Scarlato, P., 2013. The control of cooling rate on titanomagnetite composition: implications for a geospeedometry model applicable to alkaline rocks from Mt. Etna volcano. Contributions to Mineralogy and Petrology 165, 457–475. https://doi.org/10.1007/s00410-012-0817-6.

Morimoto, N., 1988. Nomenclature of pyroxenes. Mineral. Petrol. 39, 55–76.

Neave, D.A., Putirka, K.D., 2017. A new clinopyroxene-liquid barometer, and implications for magma storage pressures under Icelandic rift zones. Am. Mineral. 102 (4), 777–794. https://doi.org/10.2138/am-20175968.

Polacci, M., Arzilli, F., La Spina, G., Le Gall, N., Cai, B., Hartley, M.E., Di Genova, D., Vo, N.T., Nonni, S., Atwood, R.C., Llewellin, E.W., 2018. Crystallisation in basaltic magmas revealed via in situ 4D synchrotron X-ray microtomography. Sci. Rep. 8, 1–13.

Probst, L.C., Sheldrake, T.E., Gander, M.J., Wallace, G., Simpson, G., Caricchi, L., 2018. A cross correlation method for chemical profiles in minerals, with an application to zircons of the Kilgore Tuff (USA). Contrib Mineral Petrol 173, 23. https://doi.org/10.1007/s00410-018-1448-3.

Putirka, K.D., 1999. Clinopyroxene + liquid equilibria to 100 kbar and 2450 K. Contrib. Mineral. Petrol. 135, 151–163. https://doi.org/10.1007/s004100050503.

Putirka, K.D., 2008. Thermometers and barometers for volcanic systems. Rev. Mineral. Geochem. 69, 61–120.

Roskosz, M., Toplis, M.J., Besson, P., Richet, P., 2005. Nucleation mechanisms: a crystal chemical investigation of phases forming in highly supercooled aluminosilicate liquids. J. Non Cryst. Solids 351, 1266–1282.

Rusiecka, M.K., Bilodeau, M., Baker, D.R., 2020. Quantification of nucleation delay in magmatic systems: experimental and theoretical approach. Contrib. Mineral. Petrol. 175 (5), 47.

Shelby, J.E., 2005. Introduction to Glass Science and Technology, 2nd edition. Conwall, Padstow.

Smith, P.M., Asimow, P.D., 2005. Adiabat_1ph: a new public front-end to the MELTS, pMELTS, and pHMELTS models. Geochem. Geophys. Geosyst. 6, Q02004 https://doi.org/10.1029/2004GC000816.

Soule, S.A., 2015. Mid-ocean ridge volcanism. In: Sigurdsson, H., Houghton, B., McNutt, S.R., Rymer, H., Stix, J. (Eds.), The Encyclopedia of Volcanoes, Second edition, pp. 395–403. https://doi.org/10.1016/B978-0-12-385938-9.00021-3.

Tribaudino, M., Nestola, F., 2002. Average and local structure in P21/c clinopyroxenes along the join diopside-enstatite. European Journal of Mineralogy 14 (3), 549–555.

Ujike, O., 1982. Microprobe mineralogy of plagioclase, clinopyroxene and amphibole as records of cooling rate in the Shirotori-Hiketa dike swarm, northeastern Shikoku, Japan. Lithos 15, 281–293.

Vetere, F., Iezzi, G., Beherens, H., Cavallo, A., Misiti, V., Dietrich, M., Knipping, J., Ventura, G., Mollo, S., 2013. Intrinsic solidification behaviour of basaltic to rhyolitic melts: a cooling rate experimental study. Chem. Geol. 354, 233–242.

Vetere, F., Iezzi, G., Beherens, H., Holtz, F., Ventura, G., Misiti, V., Cavallo, A., Mollo, S., Dietrich, M., 2015. Glass forming ability and crystallization behaviour of sub – alkaline silicate melts. Earth-Science Reviews 150, 25–44.

Wang, L., Liu, B., Li, H., Yang, W., Ding, Y., Sinogeikin, S.V., et al., 2012. Long-range ordered carbon clusters: a crystalline material with amorphous building blocks. Science 337, 825.

Wieser, P.E., Kent, A.J.R., Till, C.B., Donovan, J., Neave, D.A., Blatter, D.L., Krawczynski, M.J., 2023. Barometers behaving badly I: assessing the influence of analytical and experimental uncertainty on clinopyroxene thermobarometry calculations at crustal conditions. Journal of Petrology 64 (2), egac126. https://doi.org/10.1093/petrology/egac126.